LETTER

Fuel gain exceeding unity in an inertially confined fusion implosion

O. A. Hurricane[1], D. A. Callahan[1], D. T. Casey[1], P. M. Celliers[1], C. Cerjan[1], E. L. Dewald[1], T. R. Dittrich[1], T. Döppner[1], D. E. Hinkel[1], L. F. Berzak Hopkins[1], J. L. Kline[2], S. Le Pape[1], T. Ma[1], A. G. MacPhee[1], J. L. Milovich[1], A. Pak[1], H.-S. Park[1], P. K. Patel[1], B. A. Remington[1], J. D. Salmonson[1], P. T. Springer[1] & R. Tommasini[1]

Ignition is needed to make fusion energy a viable alternative energy source, but has yet to be achieved[1]. A key step on the way to ignition is to have the energy generated through fusion reactions in an inertially confined fusion plasma exceed the amount of energy deposited into the deuterium–tritium fusion fuel and hotspot during the implosion process, resulting in a fuel gain greater than unity. Here we report the achievement of fusion fuel gains exceeding unity on the US National Ignition Facility using a 'high-foot' implosion method[2,3], which is a manipulation of the laser pulse shape in a way that reduces instability in the implosion. These experiments show an order-of-magnitude improvement in yield performance over past deuterium–tritium implosion experiments. We also see a significant contribution to the yield from α-particle self-heating and evidence for the 'bootstrapping' required to accelerate the deuterium–tritium fusion burn to eventually 'run away' and ignite.

At the National Ignition Facility (NIF), 192 lasers deliver up to 1.9 MJ of light into a gold hohlraum, a cylindrically shaped radiation cavity (Fig. 1), that converts the energy into a nearly Planckian X-ray bath. A fraction of the X-rays are absorbed by a capsule generating ~100 Mbar of pressure in the ablator (the outer shell of the capsule). This ablation pressure, delivered as a series of weak shocks, accelerates the capsule inwards. Against the inside of the ablator is the deuterium–tritium (D–T) fuel shell, which is initially in a cryogenic ice state. When the implosion achieves peak velocity, the fuel has a kinetic energy that is a fraction of the X-ray energy absorbed by the capsule. As the fuel stagnates (stops moving), abruptly arrested by the high pressures forming at the centre of the implosion, the D–T forms a hotspot from the fuel's inner surface and PdV work (pressure times volume change) is done on the hotspot. The hotspot initiates the fusion reactions, producing neutrons and α-particles as the hotspot ion temperature climbs to many kiloelectronvolts. At sufficient hotspot areal density, $(\rho r)_{hs} > 0.3 \, \mathrm{g \, cm^{-2}}$, and ion temperature, $T_{ion} > 4 \, \mathrm{keV}$ (where Boltzmann's constant has been suppressed), the hotspot will 'ignite' as α-particles redeposit their energy locally. If the fuel areal density, $(\rho r)_{fuel} > 1 \, \mathrm{g \, cm^{-2}}$ the burn will propagate (heat adjacent cold fuel, causing it also to fuse and burn) and a run-away self-heating process releases energy many times greater than that absorbed by the capsule.

Mix of the ablator and D–T can degrade the ability of an inertially confined fusion implosion to compress the D–T fuel and can also cause undesirable cooling because high-atomic-number (high-Z) materials in the D–T hotspot will rapidly radiate away energy in the form of bremsstrahlung emission, the power of emission scaling in proportion to Z^2. Among many motivations, the high-foot implosion[2,3] was developed in the wake of the National Ignition Campaign[4,5] (NIC) primarily to address the possibility that ablation-front-driven instability[6,7] was responsible for part of the observed degraded yield performance[1] and the ablator–fuel mix inferred from X-ray emissions in combination with primary neutron yield[8,9].

The high-foot implosion is designed to reduce ablation-front-driven instability growth and thereby inhibit ablator plastic (carbon–hydrogen and silicon dopants) from mixing into and contaminating the D–T hotspot. The laser pulse shape is designed to obtain a relatively high hohlraum radiation temperature ($T_{rad} \approx 90$–100 eV) during the 'foot' of the pulse (Fig. 1) and launches three shocks. In contrast, the NIC implosion pulse shape drives a lower radiation temperature ($T_{rad} \approx 60$ eV) in the foot (hence 'low-foot') for longer and launches four shocks. The essential stability benefits of the high-foot scheme can be understood from examining an expression for the linear growth rate of the ablation-driven Rayleigh–Taylor instability[10]

$$\gamma_{A-RTI} = \alpha_2(\mathrm{Fr}, \, \nu) \sqrt{\frac{kg}{1 + kL_\rho}} - \beta_2(\mathrm{Fr}, \, \nu)kv_a \qquad (1)$$

where k is the perturbation wavenumber, g is the ablator acceleration, L_ρ is the density gradient scale length of the ablation front, v_a is the ablation velocity, and α_2 and β_2 are parameters of order unity whose exact values depend on a heat conduction scale-length parameter, ν, and the Froude number, $\mathrm{Fr} = v_a^2 / (gL_\rho)$. The key stabilizing effects of the high-foot drive enter through the higher ablation velocity, which scales as $T_{rad}^{9/10}$, increasing the $\beta_2 k v_a$ ablative stabilization term of equation (1), and through an increase in L_ρ, which reduces the instability term proportional to $\sqrt{kg}$. The increase in L_ρ is primarily due to a stronger first shock, which increases the adiabat of the implosion and prevents the ablator from becoming so highly compressed (risking break-up) during the implosion. The enhanced stability can be further understood by comparing the respective in-flight aspect ratios ($R_{in}/\Delta R$, where R_{in} is the ablator inner radius and ΔR is the ablator thickness) of the high- and low-foot implosions: for the high-foot implosion, the in-flight aspect ratio is roughly half that of the low-foot implosion—the amplitude of instability growth is directly related to the exponential of $\sqrt{R_{in}/\Delta R}/2$ (ref. 11). The trade-off made to obtain the improved stability of the high-foot implosion is that the D–T fuel adiabat, $a = P/P_F$ (usually denoted α), where P is pressure and P_F is the Fermi pressure, is higher, making the fuel less compressible for a given amount of absorbed energy. (An alternate definition of the adiabat using P_{cold}, the minimum D–T pressure at 1000 g cm^{-3}, is sometimes used[12].) Details of the stability benefits, other theoretical motivations and trade-offs involved in the high-foot implosion, and the initial results from the first set of five D–T implosion experiments are described elsewhere[2,3].

Deuterium–tritium implosions N130927 and N131119 (NIF shot number in year–month–day format YYMMDD) build on the previous high-foot shot, N130812[3], by modestly increasing the NIF laser power and energy (Table 1) and by redistributing energy between different laser beams, through laser wavelength changes that affect the cross-beam transfer (the transfer of power from one beam to another via induced Brillouin scattering), to optimize the illumination pattern in

[1]Lawrence Livermore National Laboratory, PO Box 808, Livermore, California 94551, USA. [2]Los Alamos National Laboratory, Los Alamos, New Mexico 87545, USA.
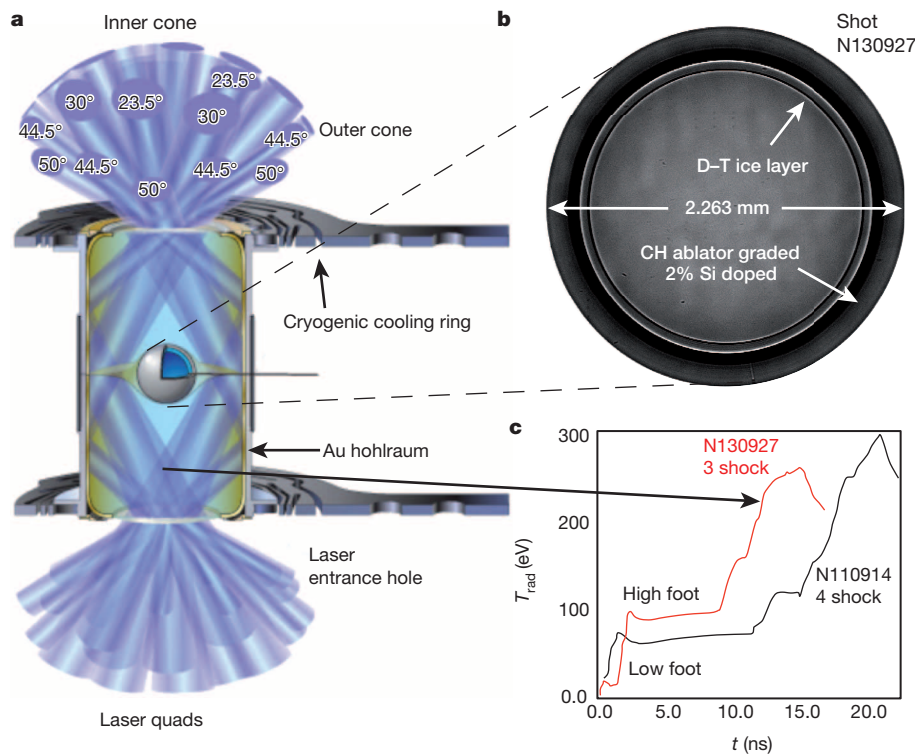
Figure 1 | Indirectly driven, inertially confined fusion target for NIF.
a, Schematic NIF ignition target showing a cut-away of the gold hohlraum and plastic capsule with representative laser bundles incident on the inside surface of the hohlraum. **b**, X-ray image of the actual capsule for N130927 with D–T fuel layer and surrounding CH (carbon–hydrogen) plastic ablator. **c**, X-ray radiation drive temperature versus time for the NIC low-foot implosion and the post-NIC high-foot implosion.

the hohlraum[13–16]. Although the hotspot shape changes that result from these wavelength changes can be predicted to some extent[17], in practice the precise wavelengths needed to achieve the desired (that is, round) shape are found empirically. For N130927, the choice of $\lambda_{23.5} - \lambda_{30} = 0.7$ Å between the 23.5° and 30.0° inner-cone beams was chosen for azimuthal symmetry control, with $\Delta\lambda_{23.5-outer} = 9.2$ Å and $\Delta\lambda_{30-outer} = 8.5$ Å (the respective laser wavelength differences between the 23.5° and 30° inner-cone beams and the outer-cone beams) used for equatorial symmetry control (see Fig. 1 for beam angles). For N131119, $\Delta\lambda_{23.5-outer} = 9.5$ Å and $\Delta\lambda_{30-outer} = 8.8$ Å. These wavelength choices were critical for keeping the hotspot shape under control as the implosion was pushed to higher velocities, because previous experiments had already shown the tendency for the hotspot to deform into an oblate toroidal shape when laser power was increased[3]. There are limits to the amount of control that can be exerted over the hotspot shape just

through wavelength changes alone, and physical changes to the hohlraum may also be required in future experiments to maintain hotspot (and fuel) shapes that will achieve the desired results.

We used a gold hohlraum of 5.75-mm diameter and 9.425-mm length, which are typical values in most high-foot cryogenic D–T implosion experiments (Fig. 1). The same hohlraum geometry was used during the NIC for most of the low-foot shots. As is typical for the high-foot series, the hohlraum was filled with helium gas of 1.6 mg cm^{-3} density (as compared with 0.96 mg cm^{-3} for the NIC), the purpose of which is to restrict and delay ingress of gold plasma from the inside wall of the hohlraum, which can impede laser beam propagation. The plastic capsule at the centre of the hohlraum for N130927 and N131119 respectively had outer-shell radii of 1.1315 and 1.1241 mm and inner-shell radii of 0.9365 and 0.9303 mm (Fig. 1). Layered on the inner surface of the capsule shell for N130927 and N131119 were 71.4

Table 1 | Measured and derived implosion performance metrics

Quantity	N131119$^{425\,TW}_{1.9\,MJ}$	N130927$^{390\,TW}_{1.8\,MJ}$	N130927[25]	N130927[26]	N130927 (sim.)
Y_{13-15} (neutron)	$(5.2 \pm 0.097) \times 10^{15}$	$(4.4 \pm 0.11) \times 10^{15}$	—	—	7.6×10^{15}
T_{ion} (keV) D–T	5.0 ± 0.2	4.63 ± 0.31	—	—	4.2
T_{ion} (keV) D–D	4.3 ± 0.2	3.77 ± 0.2	—	—	3.9
DSR (%)	4.0 ± 0.4	3.85 ± 0.41	—	—	4.1
τ_x (ps)	152.0 ± 33.0	161.0 ± 33.0	—	—	137
$P0_x, P0_n$ (μm)	$35.8 \pm 1.0, 34 \pm 4$	$35.3 \pm 1.1, 32 \pm 4$	—	—	32
$P2/P0_x$	-0.34 ± 0.039	-0.143 ± 0.044	—	—	—
$P3/P0_x$	0.015 ± 0.027	-0.004 ± 0.023	—	—	—
$P4/P0_x$	-0.009 ± 0.039	-0.05 ± 0.023	—	—	—
Y_{total} (neutron)	6.1×10^{15}	5.1×10^{15}	—	—	8.9×10^{15}
E_{fusion} (kJ)	17.3	14.4	—	—	25.1
r_{hs} (μm)	36.6	35.5	34.4–42.3	35.7–36.0	32.2
$(\rho r)_{hs}$ (g cm^{-2})	0.12–0.15	0.12–0.18	0.13–0.19	0.1–0.14	0.15
E_{hs} (kJ)	3.9–4.4	3.5–4.2	3.7–5.5	3.71–4.56	4.1
E_α (kJ)	2.2–2.6	2.0–2.4	2.0–2.4	2.0–2.5	2.8
$E_{DT,total}$ (kJ)	8.5–9.4	10.2–12.0	10.0–13.9	10.92–11.19	13.4
G_{fuel}	1.8–2.0	1.2–1.4	1.04–1.44	1.28–1.31	1.9

Lines 1–9 for columns 2 and 3 are directly measured quantities; others are derived from the data. Columns 4–6 show results from two data-driven models and simulation, respectively.
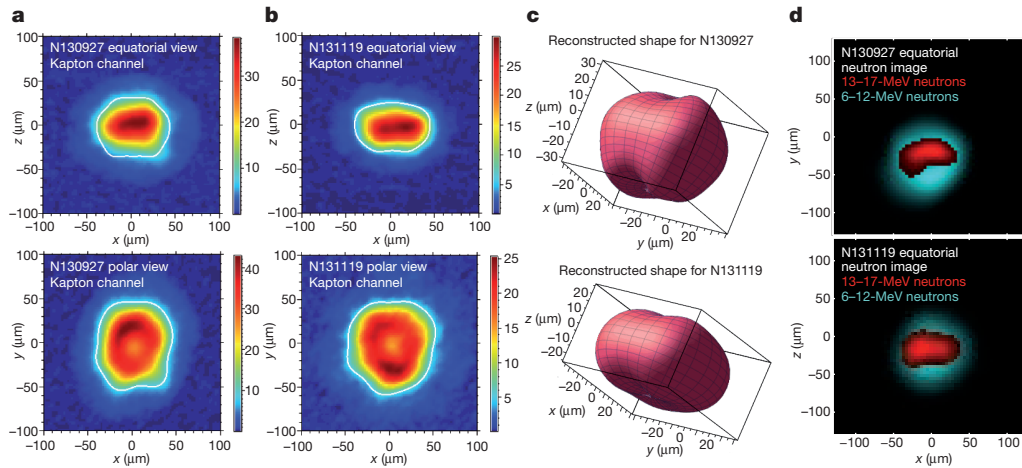
Figure 2 | X-ray and neutron images of the hotspot at bang-time.
a, Equatorial (side-on) and polar (top-down) views of the hotspot shape for
N130927. Kapton is the filter material in the imaging system that allows
transmission of X-rays with energies of more than 6 keV. **b,** As in **a**, but for
N131119. In these X-ray images, the contour shown in white is taken at the
17%-peak-brightness level (the colour scales show the brightness in arbitrary
units) and is used to obtain a description of the shape in Legendre modes

(equatorial view) and Fourier modes (polar view). **c,** Three-dimensional
reconstructions of the hotspots. **d,** Superposition of direct (13–17 MeV) and
down-scattered (6–12 MeV) neutron images from N130927 and N131119.
(X-ray image analysis courtesy of N. Izumi, S. Khan, T. Ma and A. Pak of the
NIF Shape Working Group; neutron image analysis courtesy of D. Fittinghoff,
G. Grim, N. Guler and F. Merrill of the NIF Neutron Imaging System Working
Group.)

and, respectively, 69.3 μm of cryogenic D–T ice that was held at 0.8 K
below its triple point for a shot temperature of 18.6 K, like all high-foot
D–T shots. This 'mini-quench condition' generally produces an ice
layer with fewer ice cracks than that produced by a full quench[18].
Characterization of the capsule surface showed a roughness typical
of implosion capsules for NIF, and characterization of the D–T ice
showed a roughness well within requirements. The very high quality of
the D–T ice layer on N130927 was probably not a significant factor in
its performance because the third-best shot on the NIF (N130812) had
an ice layer that was somewhat worse (with greater surface roughness)
than average. The quality of the D–T layer for N131119 was between
the qualities of the layers for N130812 and N130927.

Table 1 shows the key measurements and performance metrics for
NIF shots N130927 and N131119. Key measured quantities are the
neutron yield, Y_{13-15}, in the 13–15-MeV energy band around the char-
acteristic 14.1-MeV D–T fusion neutron energy; the burn-averaged ion
temperature, T_{ion}; the neutron and X-ray burn widths, respectively τ_n
and τ_x; the down-scatter ratio (DSR); and the time of peak neutron
brightness, or 'bang-time', t_b. On the NIF, Y_{13-15} is an average of many
diagnostics, including four neutron time-of-flight (NToF) detectors[19],
numerous radiochemical activation measurements[20] and a magnetic
recoil spectrometer[21]. The temperature T_{ion} is directly related to the
temporal spread obtained from the full-width at half-maximum of the
NToF detectors. A temporal γ-ray history gives τ_n (for the high-foot
experiments, τ_x and τ_n are consistent to within their errors). The DSR
comes from measuring, via NToF and the magnetic recoil spectro-
meter, the number of neutrons scattered into the energy range 10–
12 MeV, and is directly related to the areal density of the cold D–T fuel,
$(\rho r)_{fuel} \approx 20.3f \times DSR$ (where f depends upon the amount of ablator
mass remaining but is typically 0.95 ± 0.05 (ref. 21 and B. K. Spears,
personal communication)). Other diagnostics such as X-ray imaging
and neutron imaging (Fig. 2) give information on the shape of the
implosion.

In what follows, we will use the aforementioned observables, which
are measured over the duration of the fusion burn, to infer the amount
of energy that was deposited into the D–T (both fuel and hotspot), to
make a comparison with the amount of energy generated from fusion.
The details of the analysis will focus on N130927; the results for
N131119, which exceeded the performance of N130927, are quoted
in Table 1. The analysis outlined in this letter uses an essentially one-
dimensional 'onion-skin' picture with a hotspot of uniform density

and temperature surrounded by the fuel (with Gaussian or uniform
radial density profile), although the observed three-dimensional hot-
spot shape information is used to obtain the hotspot volume. Also, an
assumption of approximately equal ion and electron temperatures,
$T_{ion} \approx T_e$, is made and can be justified *post hoc* using an expression
for the electron–ion collision time after the hotspot density is obtained.
Analytical and simulation results based on less simplified assumptions
are also quoted in Table 1 for comparison with what is detailed below.

By analysing the observed hotspot shape (Fig. 2) in terms of Legendre
modes (equatorial view, lines 6–9 of Table 1) and Fourier modes (polar
view), where the hotspot perimeter, as defined by the 17%-of-peak-
brightness contour, is given by

$$R_{hs}(\theta) = P0 \left[1 + \sum_{\ell=2}^{\infty} \left(\frac{P\ell}{P0} \right) P_\ell(\cos\theta) \right] \qquad (2)$$

where $P_\ell(\cos\theta)$ is the Legendre function, we obtain the hotspot volume,
V_{hs} (Methods), and the effective spherical radius, $r_{hs} = (3V_{hs}/4\pi)^{1/3}$.
(We note that there is no absolute reference for the X-ray or neutron
images, and so mode $\ell = 1$ is not included in the shape description.
However, $\ell = 1$ and $m = 1$ motions can be obtained from the NToF
detectors.) The total neutron yield, Y_{total}, can be calculated from
$Y_{total} = Y_{13-15}\exp(4DSR)$, which accounts for the neutrons produced
but then scattered out of the measured 13–15-MeV energy band by
the cold and dense D–T fuel. Because for D–T fusion reactions the
energy per fusion is known (14.1 MeV per neutron and 3.5 MeV per
α-particle), E_{fusion}, the total fusion energy produced, can be calculated
from Y_{total}.

From the measured T_{ion}, the D–T reaction rate per unit volume, $\langle\sigma v\rangle$,
can be calculated using standard formulae[22] (Methods). For N130927,
$\langle\sigma v\rangle = 4.75 \times 10^{-18}$–$1.03 \times 10^{-17}$ cm^3 s^{-1} The range of values is dri-
ven by the measurement uncertainty in T_{ion}. The reported T_{ion} values
are actually averages over several detectors. The observed spread in the
individual detector T_{ion} interpretations indicates some motional
broadening contribution, which suggests that the lower temperature
is more representative of the thermal temperature. Throughout this
Letter, the uncertainty ranges given for values for all quoted quantities
are driven by the uncertainty in T_{ion}.

For a 50:50 D–T mix the fusion power density is $\dot{\epsilon}_{DT} = 7.04 \times 10^{-13}n^2\langle\sigma v\rangle$ in joules per cubic centimetre per second, where n is the
yet-unknown number density of the fusing region. From E_{fusion}, V_{hs} and

τ_x the hotspot number density can be calculated:

$$n = \sqrt{\frac{E_{\text{fusion}}}{7.04 \times 10^{-13} \langle \sigma v \rangle V_{\text{hs}} \tau_x}}$$

For N130927, $n = 8.1 \times 10^{24}$–$1.2 \times 10^{25}\,\text{cm}^{-3}$, a value that also provides the hotspot mass density (assuming a pure D–T hotspot, with average atomic mass number $\bar{A} = 2.5$ for D–T), $\rho_{\text{hs}} = 34$–$50\,\text{g cm}^{-3}$; the hotspot mass, $m_{\text{hs}} = \rho_{\text{hs}} V_{\text{hs}} = 6.4$–$9.4\,\mu\text{g}$; and the areal density, $(\rho r)_{\text{hs}}$ (Table 1).

A number of quantities describing the implosion energetics now straightforwardly follow. The hotspot pressure can be obtained from $P_{\text{hs}} = (\bar{Z} + 1) \rho_{\text{hs}} T_{\text{ion}} / \bar{A}$ ($\bar{Z} = 1$ for D–T), yielding $P_{\text{hs}} = 126$–$152\,\text{Gbar}$. The hotspot energy is then $E_{\text{hs}} = (3/2) P_{\text{hs}} V_{\text{hs}}$ (Table 1). The fraction, f_α, of α-particle energy deposited into the hotspot can be calculated from a classic formula[23]

$$f_\alpha = 1 - \frac{1}{4 \left[(\rho r)_{\text{hs}} / \rho \lambda_\alpha \right]} + \frac{1}{160 \left[(\rho r)_{\text{hs}} / \rho \lambda_\alpha \right]^3}$$

where the α-particle stopping range can be found from[24]

$$\rho \lambda_\alpha = \frac{0.025 T_e^{5/4}}{1 + 0.0082 T_e^{5/4}} \qquad (3)$$

in base units of centimetres, grams, and kiloelectronvolts. For N130927, $f_\alpha = 0.68$–0.82. The energy deposited in the hotspot by α-particles is $E_\alpha = f_\alpha E_{\text{fusion}} / 5$, recalling that one-fifth of the D–T fusion energy is emitted in the form of α-particles (the remaining α-particle energy is deposited into the cold fuel). We note that, using the values found in Table 1, $E_\alpha / E_{\text{hs}} \approx 0.56$. These energies fully describe the hotspot, but part of the implosion energy was used to compress the remaining cold D–T fuel and so we must examine the fuel to get a full picture of the implosion energy balance.

Because the D–T hotspot is formed by ablating the inner surface of the cold D–T fuel as electron conduction transports heat from the forming hotspot into the fuel, we can calculate the amount of D–T fuel remaining after the hotspot has formed because we know the initial amount of D–T ice layered onto the inside of the capsule, $m_0 = 186\,\mu\text{g}$ (for N130927): $m_{\text{fuel}} = m_0 - m_{\text{hs}} = 176$–$179\,\mu\text{g}$. The cold D–T fuel mass forms a shell surrounding the hotspot with volume $V_{\text{fuel}} = (4\pi/3)(r_{\text{out}}^3 - r_{\text{hs}}^3)$, where r_{out} is the unknown outer fuel radius. Because $m_{\text{fuel}} = 4\pi \int \rho_{\text{fuel}} r^2\, dr$ and the measured DSR provides a way to obtain the fuel density, ρ_{fuel}, from $(\rho r)_{\text{fuel}} = \int \rho_{\text{fuel}}\, dr$, by assuming a fuel profile we can solve for both the fuel layer thickness, $r_{\text{out}} - r_{\text{hs}}$, and density ρ_{fuel} (Methods). We find that

$$r_{\text{out}} - r_{\text{hs}} = 2\sigma = \sqrt{\frac{m_{\text{fuel}}}{2\pi (\rho r)_{\text{fuel}}} - r_{\text{hs}}^2} - r_{\text{hs}} \qquad (4)$$

with a Gaussian density profile

$$\rho(r) = (\rho r)_{\text{fuel}} \frac{\exp[-(r - r_0)^2 / 2\sigma^2]}{\sqrt{2\pi}\sigma}$$

where r_0 is the radius of peak fuel density. For N130927, $r_{\text{out}} - r_{\text{hs}} = 14.7$–$15.3\,\mu\text{m}$, $\rho_{\text{fuel}} = 385$–$402\,\text{g cm}^{-3}$ and $V_{\text{fuel}} = (3.0$–$3.2) \times 10^5\,\mu\text{m}^3$. The fuel outer radius from these arguments, $r_{\text{out}} = 50.8\,\mu\text{m}$ (at 50% ρ_{fuel}), is close to that obtained directly from the down-scattered neutron image (Fig. 2), where $P0 = 55.4\,\mu\text{m}$ (at 17% of maximum intensity). By this time of peak compression, the D–T fuel density has increased by a factor of more than 1,500. The fuel density is not required for calculating the fuel energy, but it can be used to estimate the adiabat of the fuel (at bang-time) assuming that the cold fuel and the hotspot are isobaric ($P_{\text{fuel}} \approx P_{\text{hs}}$), in which case we find that $a = P_{\text{fuel}} / P_F \approx P_{\text{hs}} / 0.0021 \rho_{\text{fuel}}^{5/3} = 2.9$–$3.3$ for N130927—the fuel adiabat in flight is lower than this range of values. The fuel density is also needed to calculate the X-ray losses through the fuel.

As the hotspot is compressed to high temperatures, the primary energy loss mechanism is bremsstrahlung X-ray emission because the D–T hotspot is optically thin to these X-rays. The bremsstrahlung energy loss is calculated to be[24]

$$E_{\text{brems}}\,(\text{kJ}) = 5.34 \times 10^{-34} n_{\text{hs}}^2 \sqrt{T_e} V_{\text{hs}} \tau_x$$

in base units of centimetres, kiloelectronvolts and seconds. For N130927, $E_{\text{brems}} = 2.3$–$4.5\,\text{kJ}$, the low end of which is nearly equivalent to the
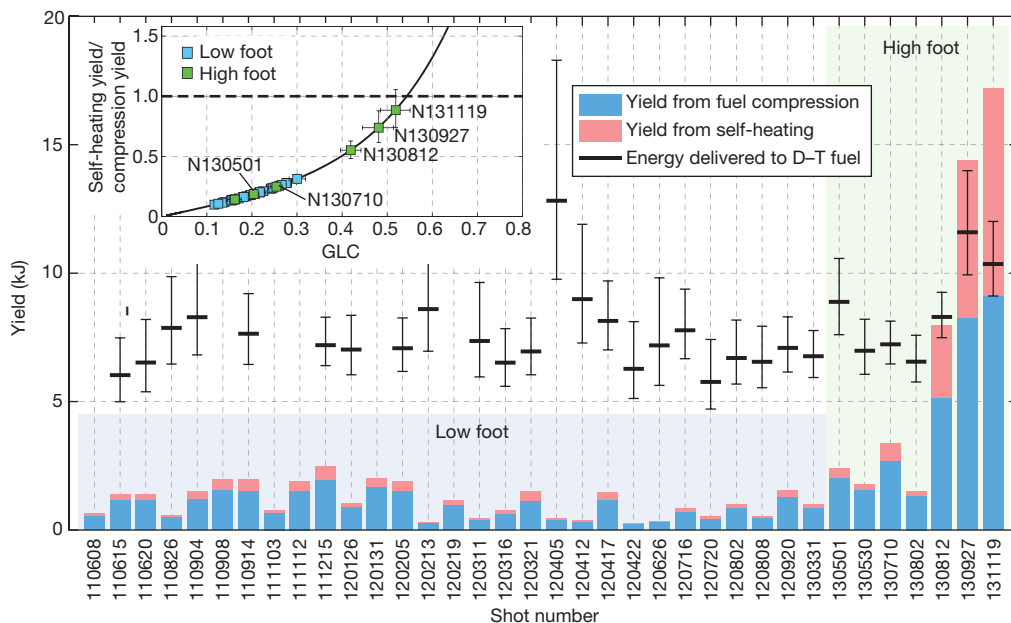
Figure 3 | Yield and energetics metrics for shots on the NIF. Total fusion yield is plotted versus shot number (that is, time). Shots 110608–130331 are low-foot shots. Shots 130501–131119 are high-foot shots. The bars showing total yield are broken into components of yield coming from α-particle self-heating and yield coming from compression. The black dashes denote the energy delivered to the D–T (fuel plus hotspot) with error bars (black vertical lines, 1σ) as calculated from the model of ref. 25. The plot shows that, even with the uncertainty in our results, shots 130927 and 131119 both yielded more fusion energy than was delivered to the D–T. Inset, ratio of self-heating yield to compression yield versus generalized Lawson criterion (GLC). All error bars, 1σ.

α-particle energy deposited. To examine whether or not these X-rays can escape the dense cold fuel, we can calculate the optical depth of the cold D–T fuel from $\tau_{fuel} = \rho_{fuel}\kappa_{DT}(r_{out} - r_{hs})$ using a simple D–T opacity model, $\kappa_{DT}(g\,cm^{-2}) = 0.352\rho_{fuel}(h\nu)^{-3.3}[1 - \exp(-h\nu/T_e)]$. We find that for X-ray energies of $h\nu \approx T_{ion} \approx T_e$, the D–T fuel layer is almost one optical depth, $\tau_{fuel} = 0.32$–0.66, implying that some bremsstrahlung X-rays deposit energy into the cold fuel whereas some escape. Electron conduction does not have a significant role in the total D–T energy loss from the cold fuel at stagnation, but is important for the hotspot energy loss.

The cold fuel energy at stagnation now follows from the isobaric assumption, $E_{fuel} = (3/2)P_{fuel}V_{fuel} = 6.9$–$7.8\,kJ$ (where we have over-estimated the fuel internal energy because typically the outer edge of the fuel has not fully stagnated even at bang-time). The total energy delivered to the D–T by the implosion is then (Table 1)

$$E_{DT,total} = E_{hs} + E_{fuel} + \frac{1}{2}e^{-\tau_{fuel}}E_{brems} - \frac{1}{2}E_\alpha \qquad (5)$$

The factors of one-half in the radiation term and the α-particle energy deposition account for having only half the energy emitted or deposited at peak burn. This total D–T energy was calculated with quantities measured around bang-time, but it represents the kinetic plus internal energy in the fuel at peak velocity in the implosion. A crosscheck of $E_{DT,total}$ is provided from calculating the fuel kinetic energy, K, using a direct measurement of implosion velocity from an earlier high-foot '1DConA' shot, N130409 (at 350 TW and 1.3 MJ of laser power and energy), where the peak ablator centre-of-mass velocity was measured to be $267 \pm 15\,km\,s^{-1}$, which is equivalent to a fuel velocity of $297 \pm 15\,km\,s^{-1}$ (the fuel being at smaller radius and convergence makes the velocity larger). Scaling the N130409-derived velocity to the laser power of N130927 (implosion velocity, $v_{imp} \propto P_{laser}^{0.41}$) gives a fuel velocity of $v_{fuel} = 311 \pm 15\,km\,s^{-1}$, and so $K = (1/2)m_0 v_{fuel}^2 = 9.0 \pm 0.9\,kJ$. The difference between K and $E_{DT,total}$ is the internal energy of the fuel at peak velocity plus the additional PdV work done by the ablator on the fuel during the deceleration.

The total fuel energy gain, $G_{fuel} = E_{fusion}/E_{DT,total}$ is now known and is 1.2–1.4 for N130927. For comparison, in Table 1 we also show results from other data-derived models of implosion energetics[25,26] that are constructed in the spirit of the above analysis but which differ in some details. A conduction-limited temperature profile in the hotspot is added to the above development in one case[25] and the other 'detailed model' case includes a three-dimensional, self-consistent physics model matched to the data[26]. To complement these analytic data-driven models, in Table 1 we also show the results from a full, one-dimensional, radiation–hydrodynamics simulation[27] of N130927, with a multifrequency X-ray drive that is calibrated to shock-timing and implosion trajectory data, without any mix model applied. The inferences from data and the computer simulation all indicate that $G_{fuel} > 1$. Moreover, we have demonstrated repeatability and improvement with the follow-on shot N131119. It should be understood, however, that $G_{fuel} > 1$ indicates only that the output fusion energy exceeds the energy deposited into the fuel. This is not the same as exceeding either the energy absorbed by the capsule (defined as the ablator shell plus D–T fuel), which absorbed $\sim 150\,kJ$ for N130927 and N131119, or the energy delivered by the laser to the target (defined as the hohlraum plus capsule), which was 1.8 MJ for N130927 and 1.9 MJ for N131119.

Key yield and energy performance metrics are graphically illustrated in Fig. 3 for N131119, N130927 and all other D–T implosions carried out on the NIF since the summer of 2011. Using a key metric for ignition, the generalized Lawson criterion[28] $\chi = (P\tau)/(P\tau)_{ign}$ (which is unity at ignition) we see (Fig. 3, inset) that for N131119 we are at the threshold of achieving yield doubling due to α-particle energy deposition.

Because most of the quantities associated with inertially confined fusion that we seek to improve to achieve ignition scale as some positive power of stagnation pressure, near-term efforts focus on increasing the

implosion speed and controlling the hotspot shape with the present fuel adiabat. As the implosion speed is increased, we will necessarily risk giving back some of the gains the high-foot implosion has made in terms of instability control. New strategies for the hohlraum will also be explored because at present hohlraum physics is limiting our ability to use the full power capability on the NIF while maintaining an acceptable hotspot shape (higher laser powers are the most direct way to increase implosion speed). Future efforts may involve more elaborate schemes to maintain control over ablator instability while recovering a lower adiabat for the fuel (for example 'adiabat shaping'[29]) or also using an alternate ablator material.

METHODS SUMMARY

Formulae for the hotspot volume and the D–T reaction rate, and a discussion of fuel density profiles, are given in Methods. Neutron image shape coefficients are also given there.

1. Edwards, M. J. et al. Progress towards ignition on the National Ignition Facility. Phys. Plasmas **20**, 070501 (2013).
2. Dittrich, T. R. et al. Design of a high-foot/high-adiabat ICF capsule for the National Ignition Facility. Phys. Rev. Lett. **112**, LJ14108 (2014).
3. Park, H.-S. et al. High-adiabat, high-foot, inertial confinement fusion implosion experiments on the National Ignition Facility. Phys. Rev. Lett. **112**, LK13998 (2014).
4. Lindl, J. D. & Moses, E. I. Plans for the National Ignition Campaign (NIC) on the National Ignition Facility (NIF): on the threshold of initiating ignition experiments. Phys. Plasmas **18**, 050901 (2011).
5. Glenzer, S. H. et al. Cryogenic thermonuclear fuel implosions on the National Ignition Facility. Phys. Plasmas **19**, 056318 (2012).
6. Bodner, S. E. Rayleigh-Taylor instability and laser-pellet fusion. Phys. Rev. Lett. **33**, 761–764 (1974).
7. Goncharov, V. N. & Hurricane, O. A. Panel 3 Report: Implosion Hydrodynamics. Report LLNL-TR-562104 (Lawrence Livermore National Laboratory, 2012).
8. Ma, T. et al. Onset of hydrodynamic mix in high-velocity, highly compressed inertial confinement fusion implosions. Phys. Rev. Lett. **111**, 085004 (2013).
9. Regan, S. P. et al. Hot-spot mix in ignition-scale inertial confinement fusion targets. Phys. Rev. Lett. **111**, 045001 (2013).
10. Betti, R., Goncharov, V. N., McCrory, R. L. & Verdon, C. P. Growth rates of the Rayleigh-Taylor instability in inertial confinement fusion. Phys. Plasmas **5**, 1446–1454 (1998).
11. Lindl, J. Development of the indirect-drive approach to inertial confinement fusion and the target physics basis for ignition and gain. Phys. Plasmas **2**, 3933–4024 (1995).
12. Haan, S. et al. Point design targets, specifications, and requirements for the 2010 ignition campaign on the National Ignition Facility. Phys. Plasmas **18**, 051001 (2011).
13. Michel, P. et al. Tuning the implosion symmetry of ICF targets via controlled crossed-beam energy transfer. Phys. Rev. Lett. **102**, 025004 (2009).
14. Michel, P. et al. Symmetry tuning via controlled crossed-beam energy transfer on the National Ignition Facility. Phys. Plasmas **17**, 056305 (2010).
15. Moody, J. D. et al. Multistep redirection by cross-beam power transfer of ultrahigh-power lasers in a plasma. Nature Phys. **8**, 344–349 (2012).
16. Callahan, D. A. et al. The velocity campaign for ignition on NIF. Phys. Plasmas **19**, 056305 (2012).
17. Marinak, M. M. et al. Three-dimensional HYDRA simulations of National Ignition Facility targets. Phys. Plasmas **8**, 2275 (2001).
18. Kozioziemski, B. J. et al. Deuterium-tritium layer formation for the National Ignition Facility. Fusion Sci. Technol. **59**, 14–25 (2011).
19. Glebov, V. Yu. et al. Development of nuclear diagnostics for the National Ignition Facility. Rev. Sci. Instrum. **77**, 10E715 (2006).
20. Bleuel, D. L. et al. Neutron activation diagnostics at the National Ignition Facility. Rev. Sci. Instrum. **83**, 10D313 (2012).
21. Gatu Johnson, M. et al. Neutron spectrometry – an essential tool for diagnosing implosions at the National Ignition Facility. Rev. Sci. Instrum. **83**, 10D308 (2012).
22. Bosch, H.-S. & Hale, G. M. Improved formulas for fusion cross-section and thermal reactivities. Nucl. Fusion **32**, 611–631 (1992).
23. Krokhin, O. N. & Rozanov, V. B. Escape of α-particles from a laser-pulse-initiated thermonuclear reaction. Sov. J. Quantum Electron. **2**, 393–394 (1973).
24. Atzeni, S. & Meyer-ter-Vehn, J. The Physics of Inertial Fusion 32, 398 (Oxford Univ. Press, 2004).
25. Patel, P. et al. Performance of DT layered implosions on the NIF. Bull. Am. Phys. Soc. **58**, abstr. NO4.00001 (2013).

26. Cerjan, C., Springer, P. T. & Sepke, S. M. Integrated diagnostic analysis of inertial confinement fusion capsule performance. *Phys. Plasmas* **20,** 056319 (2013).
27. Zimmerman, G. B. & Kruer, W. L. Numerical Simulation of laser initiated fusion. *Comments Plasma Phys. Control. Fusion* **2,** 85–89 (1975).
28. Betti, R. *et al.* Thermonuclear ignition in inertial confinement fusion and comparison with magnetic confinement. *Phys. Plasmas* **17,** 058102 (2010).
29. Goncharov, V. N. *et al.* Improved performance of direct-drive ICF target designs with adiabat shaping using an intense picket. *Phys. Plasmas* **10,** 1906–1918 (2003).

Author Contributions O.A.H. was lead scientist for the high-foot campaign, and performed two-dimensional stability modelling, and one-dimensional pre- and post-shot analysis. D.A.C. was lead scientist on hotspot shape and hohlraum strategies. D.T.C. was part of the D–T shot experiment team. P.M.C. performed VISAR data unfolds. C.C. performed three-dimensional 'detailed model' calculations. E.L.D. was lead experimenter for 1DConA (*R*(*t*) trajectory) tuning experiments and capsule re-emission (early-time symmetry) tuning experiments. T.R.D. performed initial one-dimensional capsule design, scoping, and one-dimensional pre- and post-shot simulations. T.D. was lead experimentalist on a 2DConA ablator shape experiment and was part of the D–T shot team. D.E.H. was the pulse shape design physicist and performed all two-dimensional integrated hohlraum-capsule simulations. L.F.B.H. was design physicist for keyhole (shock-timing) tuning experiments. J.L.K. was lead experimentalist for symcap (hotspot shape) tuning experiments. S.L. was lead experimentalist for the keyhole (shock-timing) tuning experiments. T.M. was lead experimentalist for several 2DConA ablator shape experiments, was part of the D–T shot team, and was lead experimentalist on shot N131119. A.G.M. was part of the 1DConA and D–T experimental teams. J.L.M. was design physicist for the re-emission experiment. A.P. was part of the D–T shot team. P.K.P. provided a hotspot model analysis and metrics plots. H.-S.P. was lead experimentalist on D–T implosion shots up to and including N130927. B.A.R. was overall lead on experiments. J.D.S. constructed model multifrequency sources normalized to tuning experiments, and performed one- and two-dimensional model scoping. P.T.S. provided a hotspot model analysis. R.T. provided 1DConA analysis and was shot experimentalist.

Author Information Reprints and permissions information is available at www.nature.com/reprints. The authors declare no competing financial interests. Readers are welcome to comment on the online version of the paper. Correspondence and requests for materials should be addressed to O.A.H. (hurricane1@llnl.gov).

METHODS

Hotspot volume formulae. Using equation (2) the volume is

$$V_{hs} = 2\pi \int_0^\pi \int_0^{R_{hs}(\theta)} R^2 \, dR \sin\theta \, d\theta$$

$$= \frac{4}{3}\pi P0^3 + \frac{4}{5}\pi P0 P2^2 + \frac{8}{105}\pi P2^3 + \frac{4}{7}\pi P0 P3^2$$

$$+ \frac{16}{105}\pi P2 P3^2 + \frac{4}{9}\pi P0 P4^2 + \frac{8}{35}\pi P2^2 P4$$

$$+ \frac{80}{693}\pi P2 P4^2 + \frac{8}{77}\pi P3^2 P4 + \frac{24}{1,001}\pi P4^3 + \cdots$$

A simple correction to this volume can be applied (by multiplying the above expression by the expression below) to include m-modes (azimuthal modes):

$$1 + \frac{3}{2}\left(\frac{M2}{M0}\right)^2 + \frac{3}{2}\left(\frac{M3}{M0}\right)^2 + \frac{3}{2}\left(\frac{M4}{M0}\right)^2$$

$$+ \frac{3}{4}\frac{M2^2 M4}{M0^3}\cos[4(\phi_2 - \phi_4)]\cdots$$

where ϕ_2 and ϕ_4 are phase offsets of m-modes 2 and 4, respectively.

Deuterium–tritium reaction rate formulae. From ref. 22

$$\langle \sigma v \rangle = C_1 \zeta^{-5/6}\xi^2 \exp\left(-3\zeta^{1/3}\xi\right)$$

in cubic centimetres per second, where

$$\xi = \frac{C_0}{T_{ion}^{1/3}}$$

$$\zeta = 1 - \frac{C_2 T_{ion} + C_4 T_{ion}^2 + C_6 T_{ion}^3}{1 + C_3 T_{ion} + C_5 T_{ion}^2 + C_7 T_{ion}^3}$$

and $C_0 = 6.6610$, $C_1 = 6.4341 \times 10^{-14}$, $C_2 = 1.5136 \times 10^{-2}$, $C_3 = 7.5189 \times 10^{-2}$, $C_4 = 4.6064 \times 10^{-3}$, $C_5 = 1.35 \times 10^{-2}$, $C_6 = -1.0675 \times 10^{-4}$ and $C_7 = 1.366 \times 10^{-5}$ when T_{ion} is expressed in kiloelectronvolts.

Deuterium–tritium fuel density profile. Assuming a different density profile changes the form of equation (4), but changes the numerical value for the fuel thickness little. For example, assuming a top-hat distribution for the fuel yields

$$r_{out} - r_{hs} = \frac{1}{2}\sqrt{3m_{fuel}/\pi(\rho r)_{fuel} - 3r_{hs}^2} - 3r_{hs}/2$$

from which we obtain $r_{out} - r_{in} = 15.5$–$16.2\,\mu m$ for N130927. The fuel density does show more sensitivity, being $\rho_{fuel} = (\rho r)_{fuel}/(r_{out} - r_{in}) = 457$–$478\,g\,cm^{-3}$ for a top-hat distribution and $\rho_{fuel} = (\rho r)_{fuel}/\sqrt{2\pi}\sigma = 385$–$402$ for a Gaussian. The Gaussian profile assumption is more consistent with simulated fuel density profiles. The lower fuel density associated with the Gaussian profile increases the inferred fuel adiabat and decreases the fuel optical depth as compared with the uniform profile. The lower fuel optical depth makes the X-ray energy contribution to equation (5) larger; that is, it gives us a more conservative contribution to the total D–T energy.

Neutron image shape analysis. For N130927, the Legendre mode shape coefficients for the down-scattered neutron image are $P0 = 55 \pm 4\,\mu m$, $P2/P0 = 1\% \pm 5\%$ and $P4/P0 = -2\%$, and for the direct image $P0 = 32 \pm 4\,\mu m$, $P2/P0 = -35\% \pm 5\%$ and $P4/P0 = 2\%$. For the N131119 down-scattered neutron image, $P0 = 50 \pm 4\,\mu m$, $P2/P0 = 0\% \pm 5\%$ and $P4/P0 = 2\%$, and for the direct image $P0 = 34 \pm 4\,\mu m$, $P2/P0 = -34\% \pm 5\%$ and $P4/P0 = 1\%$.